Proton Surface Exchange Kinetics of Perovskite Triple Conducting Thin Films for Protonic Ceramic Electrolysis Cells: $BaPr_{0.9}Y_{0.1}O_{3-\delta}$ (BPY) *vs.* $Ba_{1-x}Co_{0.4}Fe_{0.4}Zr_{0.1}Y_{0.1}O_{3-\delta}$ (BCFZY)

Jongmin Lee[1,2], Haley B. Buckner[1,2] and Nicola H. Perry[1,2,*]

[1]Department of Materials Science & Engineering, University of Illinois Urbana-Champaign, 1304 W. Green St., Urbana, IL 61801, United States of America

[2]Materials Research Laboratory, University of Illinois Urbana-Champaign, 104 S. Goodwin Ave., Urbana, IL 61801, United States of America

*Corresponding Author E-mail: nhperry@illinois.edu

Abstract

Protonic ceramic electrolysis cells (PCECs) are an attractive green H_2 production technology, given their intermediate-temperature operating range and ability to produce dry H_2. However, PCECs will benefit from development of more efficient and durable "triple conducting" anodes where steam is split, H incorporated, and oxygen evolved. In this work, we evaluated the kinetics of the steam-splitting / H incorporation reaction on $BaPr_{0.9}Y_{0.1}O_{3-\delta}$ (BPY) in comparison to the benchmark $Ba_{1-x}Co_{0.4}Fe_{0.4}Zr_{0.1}Y_{0.1}O_{3-\delta}$ (BCFZY) composition, replacing most of the transition metal elements (Co, Fe, Zr) with the lanthanide Pr. We prepared geometrically well-defined perovskite BPY and BCFZY thin films by pulsed laser deposition and performed simultaneous optical transmission relaxation and electrical conductivity relaxation measurements at 400-500 °C in 0.21 atm O_2 during switching of the steam partial pressure to isolate and compare their proton surface exchange coefficients (k). The k values of BPY were comparable to those of BCFZY and more stable over time. According to angle-resolved XPS and STEM-EDS mapping of FIB cross-sections, the surface of BPY exhibited Ba enrichment, Pr deficiency, and Si contamination. In contrast, BCFZY exhibited Ba deficiency throughout, no obvious surface segregation, and less Si contamination. The Ba segregation on the BPY film appears to have promoted steam splitting / H incorporation kinetics even though the more basic surface reacted with the acidic environmental SiO_xH_y. Faster kinetics observed on stoichiometric BCFZY vs. Ba-deficient BCFZY confirmed the benefit of a high A-site Ba concentration. This result contrasts with most work on perovskites applied in solid oxide electrolysis cell anodes, in which A-site segregation is considered deleterious for surface reaction kinetics.

Keywords

Proton Surface Exchange Kinetics, Pulsed Laser Deposition, Protonic Ceramic Electrolysis Cell, Triple Conductor, Thin Film, Electrical Conductivity Relaxation, Optical Absorption, Surface Segregation

1. Introduction

Green hydrogen production is gaining increasing interest in the transition to a carbon-neutral energy infrastructure. Protonic ceramic electrolysis cells (PCECs) are a promising electrochemical technology for green hydrogen production using waste heat at intermediate temperatures (300-600 ˚C) with a lower thermodynamic voltage requirement than low-temperature (e.g. polymer electrolyte) devices. [1–3] Further, compared to solid oxide electrolysis cells, PCECs have the advantage of producing dry, rather than humid, H_2 gas at the cathode and lower temperature operation due to the faster transport of protons vs. oxide ions. [4,5] A key need for PCECs is the development of highly active anode materials for steam splitting, with both bulk chemo-mechanical and surface chemical stability in the presence of high steam concentrations, impurities, and/or acidic gases. [2,6,7] Surface chemistry can evolve under such extreme conditions, leading to time-dependent changes in steam-splitting performance. [8] Most anode compositions are based on an ABO_3 perovskite-derived lattice with corner-sharing BO_6 octahedra. [9] Typically some degree of basicity (e.g. aided by an A-site cation with low electronegativity), multivalency (e.g. a reducible B-site cation), and oxygen non-stoichiometry (via reducibility or acceptor doping) hosted in this structure can support bulk mobility of oxide ions, protons, and electronic charge-carriers, as well as surface mass and charge transfer. [10] Systematically clarifying the underpinning roles of A vs. B site cations in perovskites' activity and particularly their stability is essential for rational development of scalable electrode compositions.

The desired process taking place at the anode of PCECs is given in Eq. 1: incoming steam is split, oxygen is evolved with liberation of electrons, and protons are incorporated into the anode's ceramic lattice where they can be transported to the solid electrolyte:

$$H_2O\ (g) \rightarrow 1/2O_2\,(g) + 2H^+ + 2e^- \quad \text{(Eq. 1)}$$

From a defect chemical perspective, this process corresponds to "hydrogenation" (Eq. 2), where steam splitting involves consumption of holes from the p-type anode, bonding of incoming protons to lattice oxide ions, and evolution of oxygen; it is a superposition of the hydration and reduction processes and takes place when hole concentrations are high relative to oxygen vacancy concentrations in triple conductors. [8]

$$H_2O\ (g) + 2O_O^{\times} + 2h^{\cdot} \rightarrow 2(OH)_O^{\cdot} + 1/2O_2\,(g) \quad \text{(Eq. 2)}$$

When hole concentrations are lower relative to oxygen vacancy concentrations, such as under intermediate pO_2 atmospheres or for more purely proton conducting compositions (e.g. the electrolyte),

the pure hydration process (Eq. 3) dominates, which does not release oxygen nor electrons; this process in isolation is less helpful for the PCEC anode due to the lack of explicit charge transfer:

$$H_2O+O_O^{\times}+v_O^{\cdot\cdot}\rightarrow 2(OH)_O^{\cdot} \text{ (Eq. 3)}$$

Equation 2 indicates that both p-type conduction and proton conduction must be supported in PCEC anodes; [10] however, the surface reaction is often a more sluggish process than bulk transport, governing efficiency for electrodes with short diffusion lengths. In this case, the proton surface exchange coefficient (k) is a key performance metric. A k value captures the catalytic activity of the electrode surface, as it is the proportionality factor (materials property) relating the interfacial proton flux to the driving force (e.g. concentration gradient). Although a handful of perovskite-derived anode compositions have been demonstrated in the context of cell performance targeting primarily steam electrolysis, their k values have very rarely been quantified and reported [6]. In light of this knowledge gap, it is essential to develop an understanding of how composition relates to k, to enable rational development of electrode compositions and structures.

Among reports, $BaCo_{0.4}Fe_{0.4}Zr_{0.1}Y_{0.1}O_{3-\delta}$ (BCFZY) is an established potential steam electrode candidate [11,12], with a reported proton exchange k value of 3.85×10^{-6} cm/s at 500 ˚C in 0.21 atm pO_2. [13] This value was measured by the pH_2O-switching electrical conductivity relaxation (ECR) technique on a bulk porous BCFZY ceramic, assuming negligible contribution from bulk diffusion; however, the surface area was unknown. In general, ill-defined porous ceramic electrodes complicate quantitative analysis of surface exchange kinetics due to various thickness, morphological, and geometry effects. Those can lead to larger uncertainty in the k values and difficulty comparing among samples where both composition and microstructure differ. Dense ceramics with known surface areas can also be difficult to analyze for surface exchange kinetics by relaxation methods, because typically then the bulk diffusivity (D) plays a non-negligible role in observed kinetics. Fitting for both D and k simultaneously may introduce uncertainty in materials with one mobile ion, but the time-dependent responses for triple conductors with multiple diffusing species can be even more complex. For example, multiple conductivity relaxations in opposite directions can be superimposed, requiring careful fitting and analysis. [14,15] Therefore, a geometrically well-defined electrode structure that avoids diffusion contributions to the kinetic response is preferred.

Dense, thin-film samples can support both surface exchange-limited kinetics and well-defined surface areas for direct comparison of different compositions' performance. [16] Pulsed laser deposition (PLD) is a useful growth technique for preparing dense, complex compositions with a high degree of control over structure across length scales. [17] Another benefit of the thin-film geometry is ability to measure simultaneous ECR/optical transmission relaxation (OTR), which has previously been applied to study

oxygen reduction/evolution reactions on mixed ionic/electronic conductor (MIEC) thin films. [18] The OTR technique measures optical transmission relaxations, leveraging a linear relationship between defect concentration and optical absorption at a key wavelength; as a contact-free method, by itself it eliminates concerns about the catalytic contribution of metal current collectors. [19] However, by using buried electrodes (under the film, away from the film-gas interface), simultaneous *in-situ* OTR/ECR measurements can also determine reliable k values and, moreover, insight into the nature of the kinetic response or dominant reaction (e.g. Eq. 2 vs. Eq. 3). In prior work on (MIEC) perovskite thin film electrodes, oxygen exchange k values have been studied and evaluated by ECR and/or OTR. [18,20,21] However, there are no reports yet on the proton exchange k values of triple-conducting thin films by any method to the best of our knowledge. Growth of BCFZY thin films by PLD has been reported, but the thin-film k values have not been investigated yet. [22]

Our aims in this work were to a) measure proton exchange k values on thin-film triple conducting oxides for the first time, leveraging simultaneous OTR/ECR and the well-defined geometry, and b) gain insight into the impact of composition on k, by systematically altering the B-site composition and A-site occupancy and observing evolution of surface chemistry in each case. BCFZY was chosen as a reference composition. Because of its high number of cations and Ba volatility, both the synthesis and analysis of precise stoichiometry in BCFZY are difficult, given overlapping peaks in various spectroscopy methods. [11,23] We nonetheless were able to prepare films with differing levels of Ba sub-stoichiometry on the A-site for comparison of k values and to confirm bulk and surface stoichiometry across various techniques. We also selected the simpler composition $BaPr_{0.9}Y_{0.1}O_{3-\delta}$ (BPY) as a comparator, in which the transition metals Co, Fe, and Zr on the B-site are replaced by the lanthanide Pr. BPY maintains the low electronegativity of the A-site cation but alters the reducibility of the B-site cation, with the same nominal acceptor (Y) concentration. The more comparable volatility of Pr and Ba may assist in forming stoichiometric electrodes. Pr-oxides have been applied in the context of surface coatings for MIEC oxygen exchange [24], as single-phase MIECs demonstrating sensitivity to Si poisoning [25], and in PCEC electrodes tested under high steam contents [26,27]. $BaPrO_{3-\delta}$ with various B-site acceptor dopants such as Gd, Yb, and Y was reported as a potential triple conductor (holes, oxide ions, protons), [28,29,30] and thin films of $BaPrO_{3-\delta}$ that supported both protonic and electronic conductivity apparently hosted multivalent $Pr^{3+/4+}$ which contributed to oxygen vacancy formation. [31,32,33] In prior work, we also demonstrated that BPY can undergo oxygen exchange, where it has an anomalously low redox coefficient of chemical expansion, [34] which may aid chemo-mechanical stability.

In this work, we grew dense BPY and BCFZY thin films by PLD on various substrates and measured the proton exchange k at 400-500 °C by simultaneous OTR/ECR. As mentioned, while ECR has

been applied in very limited studies to evaluate hydrogenation kinetics on bulk ceramics, the OTR method was applied for the first time here in the context of H_2O splitting / H incorporation analysis on triple conductors. The electrical and optical relaxation responses upon introduction of H_2O were consistent with hydrogenation, where holes are consumed. The BPY thin films exhibited relatively higher proton exchange *k* and more stable, repeatable relaxation behavior over time than the BCFZY thin films. To understand the difference in proton surface exchange kinetics between BPY and BCFZY, the surface morphology, structure, and surface vs. bulk compositions were characterized before and after relaxation measurements through atomic force microscopy, X-ray diffraction, Rutherford backscattering spectrometry (RBS), angle-resolved X-ray photoelectron spectroscopy, and scanning transmission electron microscopy (STEM) with energy-dispersive X-ray spectroscopy (EDS). BPY exhibited a stoichiometric bulk composition with significant Ba segregation to the surface; this basic surface reacted with acidic SiO_x from the quartz tube during OTR/ECR, and the surface morphology coarsened dramatically. Despite these changes, the *k* values were higher and more stable. BCFZY typically exhibited a Ba-deficient bulk composition, which gave rise to a more stable surface chemistry and morphology over time; however, its steam-switching optical/electrical relaxation behavior was unstable and slower. Preparation of more stoichiometric BCFZY with higher Ba content resulted in higher *k* values. For both compositions, the choice of (inert) substrate played a role in *k*. These results suggest that: a) multivalent transition metals are not required for good proton exchange *k* values since Pr works well in place of Fe and Co; b) a highly basic surface rich in the A-site cation seems beneficial even though it reacts with impurities; and c) substrate-induced effects play a role in the *k* values.

2. Experimental methods

2.1. PLD target fabrication

BPY and BCFZY PLD ceramic targets were prepared by a modified Pechini method [34] as described in the following. After determining the H_2O content of each nitrate precursor via mass loss analysis, calculated amounts of $Ba(NO_3)_2$ (99.999%, Alfa Aesar), $Pr(NO_3)_3$ (99.9%, Alfa Aesar), $Y(NO_3)_3$ (99.99%, Alfa Aesar), $Co(NO_3)_2$ (99.999%, Alfa Aesar), $Fe(NO_3)_3$ (99+%, Acros Organics), and/or $Zr(NO_3)_3$ (99.9%, Thermo Scientific Chemicals) were dissolved into deionized water for at least 30 mins with stirring. Citric acid (Fisher Chemical) was added into the solution at 60 ˚C according to a citric acid: total metal cation molar ratio of 3:1. The pH of the solution was balanced to ~ 6 with pH meter paper (HYDRION, pH 0.0 – 13.0) using ammonia solution additions. Then, ethylene glycol (Fisher Chemical) was added. The addition of citric acid and ethylene glycol plays a role in formation of a polymer network with trapped metal ions. The

solution was stirred and heated to become a viscous gel for ~ 6 hours at ~ 105 ˚C, measured by mercury thermometer on the hot plate. The gels then underwent further drying to remove excess water for 18 hours at a setting temperature of 225 ˚C in a muffle furnace (Thermolyne^{TM}, Thermo Scientific) within the fume hood. The dried sponge-like gels were transferred to alumina crucibles for calcination at 800 and 700 ˚C for the BPY and BCFZY powders, respectively, in the muffle furnace to remove most of the organics. The powders were then re-ground using a mortar and pestle for uniaxial pressing into approximately 1.1 inch diameter pellets at 125 MPa. The BPY and BCFZY green targets were sintered in air at temperatures of 1400 and 1200 ˚C, respectively, for 10 and 5 h, respectively, in a box furnace inside a bed of sacrificial powder of the same compositions and with nested alumina crucibles with lid to lessen Ba evaporation. The heating/cooling rates were 2 ˚C/min during the sintering process.

2.2. Thin film growth and structural characterization

BPY and BCFZY thin films were grown on double-side polished single crystalline *c*-Al_2O_3 (0001) substrates (MTI Corporation) using pulsed laser deposition (PLD) with a KrF (248 nm) ultraviolet excimer laser (Lambda Physick, LPX 210) in 35 mtorr of O_2 (base pressure: 0.003 mTorr) at 700 ˚C. The deposition took place by rastering the laser on the target, with a repetition rate of 5 Hz and a laser energy of ~350 mJ (in the laser) / 0.09 ~0.1 W at the intelligent window entering the chamber, with a target-to-substrate distance of 55 mm, and rotation of the substrate at 5 rpm (PVD Products, Inc.). The film growth rates and thicknesses were calibrated and verified by X-ray reflectivity (Bruker, D8 Advance) and Rutherford Backscattering Spectrometry (RBS, Pelletron Accelerator). The films' crystalline phases and orientations were measured by out-of-plane X-ray diffraction (Bruker, D8 Advance) coupled 2theta-omega scans, in Bragg–Brentano geometry with Cu Kα (~1.54 Å) radiation. Film surface topographies were scanned in tapping mode by atomic force microscopy (AFM, Asylum Research – Oxford Instruments, MFP-3D SPM); topographic plots and root mean square roughnesses were processed and calculated by Gwyddion free SPM data analysis software.

2.3. Thin film compositional characterization

For chemical analysis, RBS (NEC Pelletron Accelerator), angle-resolved X-ray photoelectron spectroscopy (XPS, Kratos Axis ULTRA), X-ray fluorescence spectrometry (XRF, Shimadzu EDX-7000), and (scanning) transmission electron microscopy with energy dispersive X-ray spectroscopy (S/TEM-EDS) measurements were performed to analyze the elemental compositions at various depths, on both as-prepared films and films after elevated-temperature measurements. From RBS spectra, the elemental concentrations and thicknesses of the BPY and BCFZY thin films were estimated using SIMNRA software, assuming target densities for BPY and BCFZY of 5.622 and 6.05 g/cm^3, respectively, which are their bulk theoretical mass

densities. XPS data analyses were carried out with CasaXPS software [35], where the binding energies were adjusted with respect to the C 1*s* reference peak, set to 284.8 eV [36]. For S/TEM-EDS sample preparation, a ~10 nm layer of Au was sputtered (Emitech Inc., USA) onto the surface of the processed films to prevent charging. Then, an additional 2.5 μm Pt surface protection layer was deposited over a region of interest (ROI), and cross sections from the ROIs were prepared for S/TEM and EDS using a lift out technique in a dual-beam focused ion beam/scanning electron microscope (Scios 2 FIB/SEM, ThermoFisher Scientific, USA). The cross sections were cut out, transferred, and thinned with a 30 kV Ga-ion beam, and further thinning and polishing was carried out at lower energy (5 kV, 2 kV) to reduce beam damage. The microstructure and composition were evaluated with a Talos F200X G2 S/TEM (ThermoFisher Scientific, USA) operated at 200 kV using a Ceta-M camera (ThermoFisher Scientific, USA), high angle annular dark field (HAADF) detector, and a 4-crystal Super-X EDS detection system (ThermoFisher Scientific, USA).

2.4. *In-situ* optical and electrical relaxation measurements

A schematic of the sample geometry and *in-situ* Optical Transmission Relaxation and Electrical Conductivity Relaxation (OTR/ECR) measurements system is given in **Figure S1**. Prior to simultaneous OTR/ECR measurements, two Pt strip current collectors with a ~2 mm gap were deposited by RF-sputtering (AJA Sputter Coater) on each substrate, and the current collectors were then coated by the PLD-deposited BPY and BCFZY thin films. This buried current collector geometry was chosen to avoid the contribution of the Pt metal-film-gas interfaces on observed reaction kinetics, [18,20] and to thereby isolate the film-gas interface response; the buried geometry may also lessen Pt diffusion. [19] Pt wires were attached to the current collectors for connection with an impedance analyzer (ModuLab Xm, Solartron) using Ag paste. Each thin film sample was positioned in the center of a quartz tube within a custom tube furnace with windows (MELLEN Company). Chopped and collimated 442 nm filtered light passed through the thin film sample, and two photodetectors monitored the incident (I_1) and transmitted (I_2) light intensities. The I_1 and I_2 intensities were synchronized via lock-in amplifiers (Model SR830 DSP Lock-In Amplifier) to reduce contributions from background light fluctuations and were recorded using a custom LabView software program. Simultaneously the in-plane electrical resistances of the thin films were measured at constant frequencies of 1 and 5 Hz and ac amplitude of 100 mV using the impedance analyzer, after determining that this frequency adequately captures the dc resistances at each temperature and gas atmosphere in the study using complete impedance spectra over the frequency range 10^6-10^{-1} Hz. Oxygen partial pressure (pO_2) (21%O_2) and water partial pressure (pH_2O) (~2.3% via flowing the Ar/O_2 gas through a water bubbler held at ~ 20 ˚C vs. ~0% via avoiding the bubbler) were controlled by mass flow controllers (ALICAT SCIENTIFIC) and switched through a four-way valve equipped with bubbler and water bath (HAAKE SC 100, Thermo Scientific). For the OTR/ECR experiments at 21%O_2/Ar to determine proton surface exchange

coefficients, the pH_2O was stepped quickly by switching the 4-way switch to change to the gas stream from the nominally dry stream to that coming from the bubbler. Only the dry → humid condition was used for quantitative analysis, since the gas switch is very rapid (<5 s); the tube takes considerably longer to return to the "dry" state after H_2O introduction, and so the humid → dry relaxations were not analyzed quantitatively.

3. Results and discussion

3.1 As-Grown Film Structure

The BPY and BCFZY thin films were prepared on optically inert and electrically insulating sapphire or MgO substrates, with the sapphire case shown schematically in **Figure 1(a)**. The buried Pt current collectors for ECR measurements were deposited by DC-sputtering at a room temperature to a thickness of ~100 nm prior to BPY and BCFZY thin film growth. To assess the crystalline phase and crystallographic orientations of the BPY and BCFZY thin films, X-ray diffraction out-of-plane 2theta-omega scans were performed, as shown in **Figure 1(b)**. Only the Bragg diffraction peaks of BPY and BCFZY crystalline phases, platinum current collector, and *c*-Al_2O_3 single-crystal substrate were observed, without secondary phases. The XRD patterns of BPY and BCFZY PLD targets are shown in **Figure S2**. On sapphire, the (121) and (242) reflections were the strongest observed for the 700 ˚C-grown BPY thin film, suggesting a primary (121) out-of-plane orientation, with hints of (100) and (001) out-of-plane orientations observed in very minor (200) and (020) peaks. Note that the (200), (002), (121) Bragg diffraction peaks are positioned within a narrow 2θ range of ~0.2˚. The film Bragg diffraction peak positions are reasonably matched with those of $BaPrO_{3-\delta}$ thin films in the literature. [32,37] For the BCFZY thin film on sapphire, (110), (211), (220), and (311) Bragg reflections were observed, suggesting a polycrystalline film without strongly preferred orientation. The peak positions are also similar with those of a BCFZY thin film grown by PLD in literature. [22] **Figure 1(c),(d)** display the surface morphologies of as-deposited BPY and BCFZY thin films on sapphire, having RMS roughness values of ~0.57 nm (BPY) and ~1.1 nm (BCFZY). The AFM images also suggest that the BPY and BCFZY thin film surfaces feature sub-50 nm grains, with a slightly larger apparent grain size for BCFZY (Mean grain size of ~ 40.9 nm) vs. BPY (~ 33.3 nm), as-grown. For characterization of both thin films grown on MgO substrates instead, see Figure S3.

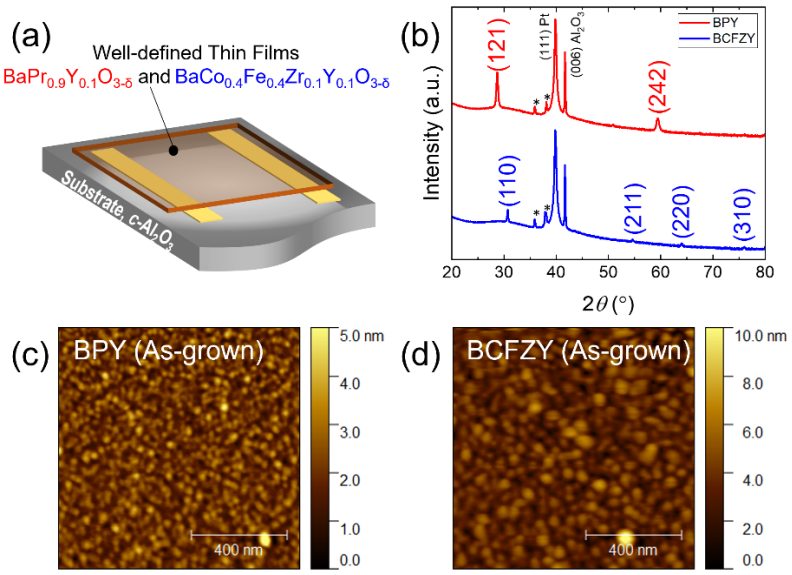

Figure 1 (a) Schematic of well-defined thin film structure with Pt current collector underneath. X-ray diffraction patterns (b) and topographic surface atomic force microscopy images with scan size of 1 μm^2 (c),(d) of BPY and BCFZY thin films on (0001) sapphire substrates, as-deposited. Asterisks indicate the diffraction peaks of the $(111)_{Pt}$ reflected by residual Cu_kβ (λ = 1.392 Å) and W_Lα (λ = 1.4767 Å) radiation in Figure 1(b). For as-deposited films on MgO substrates instead, see **Figure S3**.

3.2. Optical/Electrical Relaxation Results

Through simultaneous electrical and optical measurements, we obtained *k* values from different techniques, providing robust values, and we gained insight into the process taking place in the films as the pH_2O is increased (e.g., hydrogenation vs. hydration). **Figure 2(a)-(d)** show example OTR and ECR curves of the BPY and BCFZY thin films on sapphire, over time at a temperature of ~ 400 ˚C. Further relaxation data for different thicknesses, substrates, replicates, and temperatures are shown in the Supporting Information (Figures S4-S12). Upon increasing the pH_2O, the optical transmission and the resistance both increased. Considering that the films are p-type, both the optical and electrical relaxation directions are consistent with a reduction in hole concentration in the presence of H_2O. Further discussion of optical changes is provided in the Supporting Information. We observed OTR curves for five times upon switching steam from 0% to 2.3% pH_2O in the BPY thin film as shown in **Figure 2(a)**. However, only the first OTR curve of BCFZY thin film was observed in response to steam exchange, because the kinetics became too slow as the film aged, as shown in **Figure 2(b)**. The ECR curves of BPY and BCFZY thin films corresponded with those in the OTR curves, as shown in **Figure 2(c),(d)**, respectively. The BPY thin film exhibited relatively high

resistances at ~ 400 ˚C due to the buried ~ 2 mm distance of the Pt current collector, leading to the noisy data due to the measurement limitation of the impedance analyzer. At ~500 ˚C, the BPY thin film resistance data show clear electrical relaxation curves; see Figure S8(c). The repeatable steam-switching behavior indicates that the BPY thin film was more catalytically stable than BCFZY thin film in terms of proton exchange. To quantify *k* values for the BPY and BCFZY thin films, we analyzed the OTR and ECR curves based on the following equations (1)-(3) for OTR and (4)-(6) for ECR, appropriate for surface exchange-limited kinetics in the linear regime; example resulting *k* values are plotted in **Figure 3**. For the fitted relaxation curves, see Figures S9 and S10.

$$g(t) \equiv \frac{\ln I(t) - \ln I(0)}{\ln I(\infty) - \ln I(0)} = 1 - e^{-t/\tau} \quad (1)$$

$$-\frac{t}{\tau} = \ln(1 - g(t)) \quad (2)$$

$$k_{\text{chem}} = \frac{L}{\tau} \quad (3)$$

where $I(0)$ is the initial light transmittance intensity prior to steam switching to 2.3% pH_2O, $I(\infty)$ is the final light transmittance intensity after the relaxation, $I(t)$ is the transmitted light intensity over time, τ is the time constant, and L is the thin film thickness.

$$h(t) \equiv \frac{1/R(t) - 1/R(0)}{1/R(\infty) - 1/R(0)} = 1 - e^{-t/\tau} \quad (4)$$

$$-\frac{t}{\tau} = \ln(1 - h(t)) \quad (5)$$

$$k_{\text{chem}} = \frac{L}{\tau} \quad (6)$$

where $R(0)$ is the initial resistance prior to steam switching to 2.3% pH_2O, $R(\infty)$ is the equilibrated resistance after the relaxation, $R(t)$ is the instantaneous resistance, τ is the time constant, and L is the thin film thickness. The resistances were recorded at low frequency impedance real-axis-intercepts that correspond to the thin film's DC resistance, *R*.

The fitted *k* values of all the BPY and BCFZY thin films are summarized in **Table 1**. Considering the initial data on sapphire at 400 °C, the first *k* value of the BPY thin film was approximately 10 times higher than that of the BCFZY thin film, although the BPY thin film exhibited a slight decrease in the *k* values over time. There are very limited *k* values for the benchmark BCFZY in the literature from porous bulk ceramics [13], and if those are extrapolated to 400 °C they would exceed the *k* values for the dense BCFZY film in this work. Slight compositional deviation in the BCFZY film from the nominal composition, discussed later, may be responsible, or the gas-facing current collectors or less-defined surface area and thickness in the

previous work may play a role. On the other hand, the higher *k* values of BPY thin films in this work are comparable to those of extrapolated bulk BCFZY from the previous report. [13] Although we were not able to extract the *k* values for either composition at the higher temperature of 500 ˚C due to the time constant of the surface reaction becoming comparable to or faster than the gas flush time, the *k* values were certainly above ~ 2.5×10^{-6} cm/s, which was the upper limit of measurable *k* value based on the film thicknesses of ~ 100 nm and gas flush time of ~ 4 s. The corresponding measured relaxations displaying very fast responses at 500 °C are shown in Figures S8, S11, and S12. We also observed an effect of substrate on the *k* values, with films on MgO exhibiting slightly faster surface proton exchange than those on *c*-Al_2O_3, with this effect present for both BPY and BCFZY films.

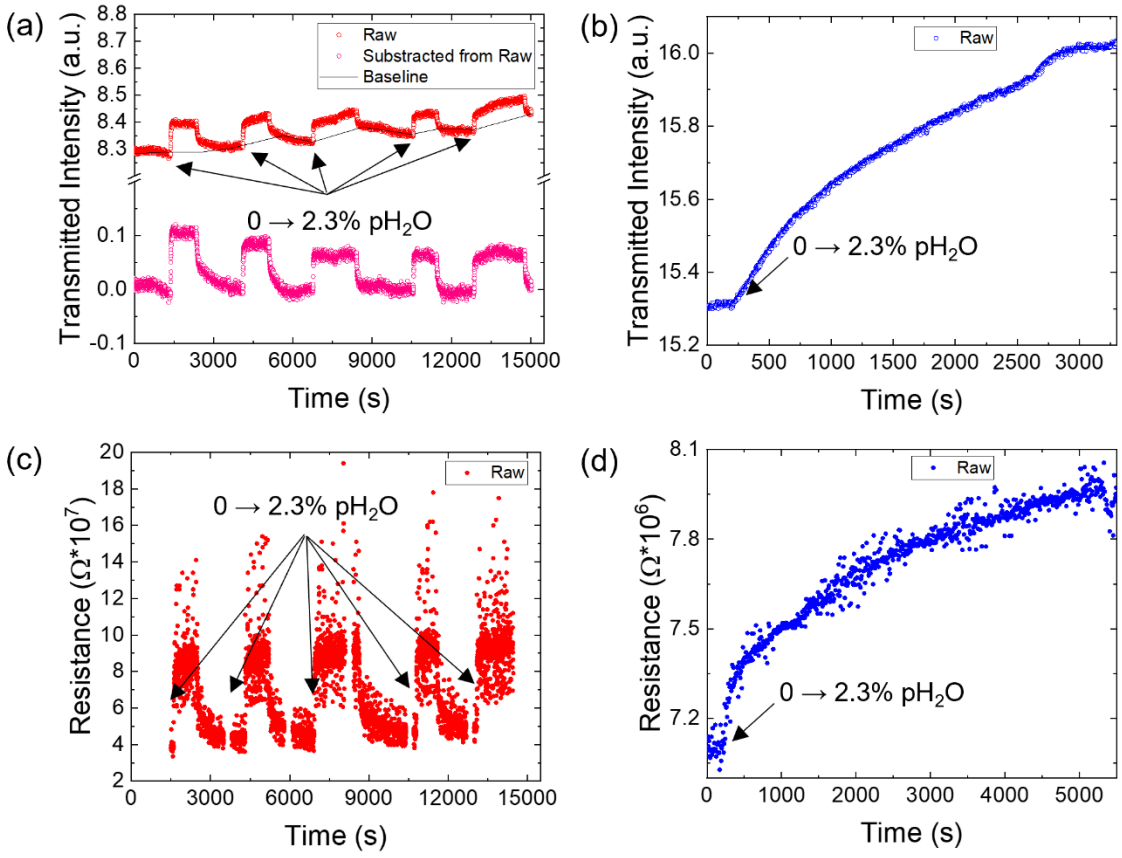

Figure 2 OTR and ECR curves upon pH_2O switching as a function of time for the BPY (a),(c) and BCFZY (b),(d) thin films on sapphire at a constant temperature around ~ 400 ˚C. (The relaxations corresponding to ~ 500 °C are given separately in Figure S8.)

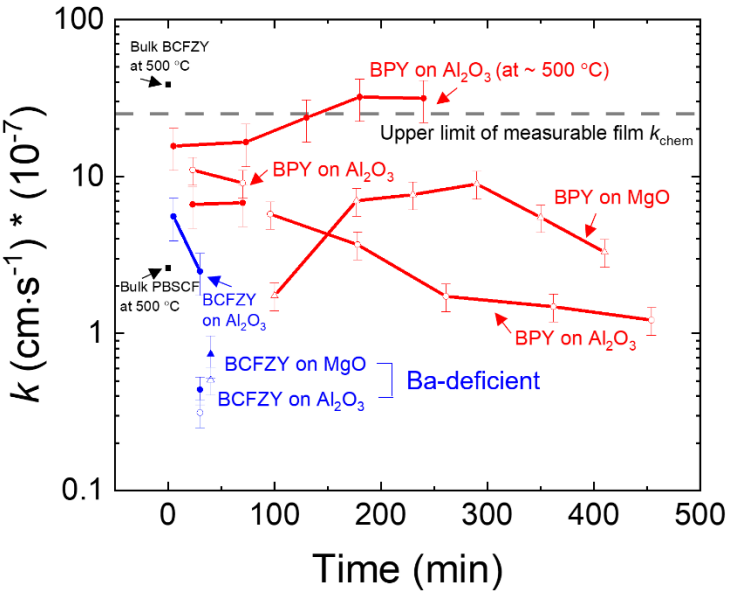

Figure 3 Comparison of proton surface exchange coefficients (k) of BPY and BCFZY thin film electrodes at a temperature of ~ 400 ˚C in our work, unless noted otherwise. Open and closed symbols indicate the k values from OTR and ECR curves, respectively. The upper limit of measurable k value in this work is $2.5*10^{-6}$ cm/s, due to the finite gas flush time, which was calculated using the following equation: $k_{chem} = L/t_{flush}$. (L = 100 nm film thickness and t_{flush} is up to 4 s). Reported bulk ceramic proton exchange k values from two literature studies at higher temperatures are included. Bulk BCFZY data from ref. [13] and bulk PBSCF ($PrBa_{0.5}Sr_{0.5}Co_{1.5}Fe_{0.5}O_{5+\delta}$) data from ref. [38].

Table 1 Comparison of proton-exchange k_{chem} values of the BPY and BCFZY thin films.

Thin film samples	k_{chem} (cm/s)	
	OTR	ECR
BPY thin film grown on Al_2O_3 (measured at ~ 400 ˚C) *replicate	$1.10*10^{-6} \pm 2.2*10^{-7}$	$6.64*10^{-7} \pm 1.99*10^{-7}$
	$9.08*10^{-7} \pm 1.82*10^{-7}$	$6.80*10^{-7} \pm 2.04*10^{-7}$
BPY thin film grown on Al_2O_3 (measured at ~ 400 ˚C)	$5.76*10^{-7} \pm 1.15*10^{-7}$	Noisy data
	$3.68*10^{-7} \pm 7.35*10^{-8}$	
	$1.72*10^{-7} \pm 3.45*10^{-8}$	
	$1.48*10^{-7} \pm 2.96*10^{-8}$	
	$1.22*10^{-7} \pm 2.43*10^{-8}$	
BPY thin film grown on MgO (measured at ~ 400 ˚C)	$1.74*10^{-7} \pm 3.48*10^{-8}$	No measurements
	$7.00*10^{-7} \pm 1.40*10^{-7}$	
	$7.66*10^{-7} \pm 1.53*10^{-7}$	
	$8.96*10^{-7} \pm 1.79*10^{-7}$	
	$5.48*10^{-7} \pm 1.10*10^{-7}$	
	$3.30*10^{-7} \pm 6.6*10^{-8}$	
BPY thin film grown on Al_2O_3 (measured at ~ 500 ˚C; probably gas-flush-time-limited)	$8.5*10^{-6} \pm 1.7*10^{-6}$	$1.56*10^{-6} \pm 4.69*10^{-7}$
	$1.24*10^{-6} \pm 2.48*10^{-7}$	$1.65*10^{-6} \pm 4.96*10^{-7}$
	$5.3*10^{-6} \pm 1.06*10^{-6}$	$2.37*10^{-6} \pm 7.10*10^{-7}$
	$6.45*10^{-6} \pm 1.29*10^{-6}$	$3.20*10^{-6} \pm 9.61*10^{-7}$
	$3.9*10^{-6} \pm 7.8*10^{-7}$	$3.14*10^{-6} \pm 9.42*10^{-7}$
BCFZY thin film grown on Al_2O_3 (measured at ~ 400 ˚C)	$3.13*10^{-8} \pm 6.26*10^{-9}$	$4.39*10^{-8} \pm 8.78*10^{-9}$
20 Hz deposited BCFZY thin film (~ 50 nm) grown on Al_2O_3 (measured at ~ 400 ˚C)	Noisy data	$5.57*10^{-7} \pm 1.67*10^{-7}$
		$2.49*10^{-7} \pm 7.46*10^{-8}$
BCFZY thin film grown on MgO (measured at ~ 400 ˚C)	$5.07*10^{-8} \pm 1.01*10^{-8}$	$7.41*10^{-8} \pm 2.22*10^{-8}$
BCFZY thin film grown on Al_2O_3 (replicate) (measured at ~ 500 ˚C)	$5.85*10^{-9} \pm 1.17*10^{-9}$	$3.74*10^{-9} \pm 1.12*10^{-9}$
	$3.36*10^{-9} \pm 6.72*10^{-10}$	-

3.3. Understanding the Behavior: Chemical and Structural Analysis Before vs. After Relaxation Testing

To interrogate surface exchange kinetics differences between fast, relatively stable BPY and sluggish, quickly degrading BCFZY thin films, we performed topographic surface AFM, cross-sectional STEM-EDS measurements, and XRD, before vs. after relaxation measurements, as shown in **Figures 4-7** and Figure S13. The topographic AFM images of both BCFZY and BPY thin films demonstrated significant changes in surface morphology after relaxation measurements, as shown in **Figure 4**. Grain coarsening is evident, and the calculated RMS surface roughnesses of ~ 6.68 nm (BPY) and ~ 4.58 nm (BCFZY) after relaxation measurements were significantly larger than the as-grown values listed in section 3.1. These results imply that heating to 400 ˚C, exposure to steam, or both led to significantly altered surfaces compared to the as-grown films. However, although BPY was deposited with a smaller initial apparent grain size, considerably larger surface features were evident on BPY post-relaxation compared to BCFZY.

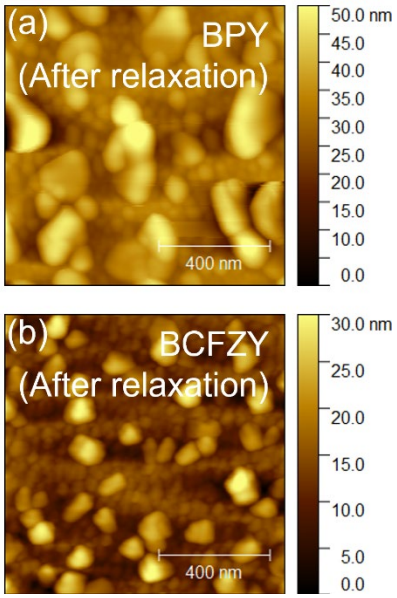

Figure 4 Topographic AFM surface images of BPY (a) and BCFZY (f) thin films on sapphire (0001) after relaxation measurements.

From the BPY transmission electron micrographs (taken after relaxation measurements), shown in **Figure 5(a),(b)**, we observed dense, 80 nm-thick films. There was a notable ~10 nm-thick region at the surface of the film with a difference in contrast in the bright field micrograph (**Figure 5(a)**), indicating that the surface phase differs from that of the bulk of the film. To gain more insight into the cation distribution through the thickness of the film, we performed STEM EDS measurements on this cross-section. From STEM EDS measurements, elemental maps for Si, Ba, and Pr are shown in **Figure 5(c)-(e)**, and a line

scan across the surface of the film is shown in **Figure 5(f)**. The outermost surface of the BPY film was clearly comprised of Si and Ba with noted depletion of B-site cations Pr and Y. Using the EDS K_α lines for quantification, the A- to B-site ratio ([Ba]:[Pr+Y]) at the surface was nominally 2:1, while the ratio approached the ideal 1:1 ratio in the bulk of the film. The Si contamination at the surface likely arose during the OTR/ECR measurement period in a quartz tube with steam switching.

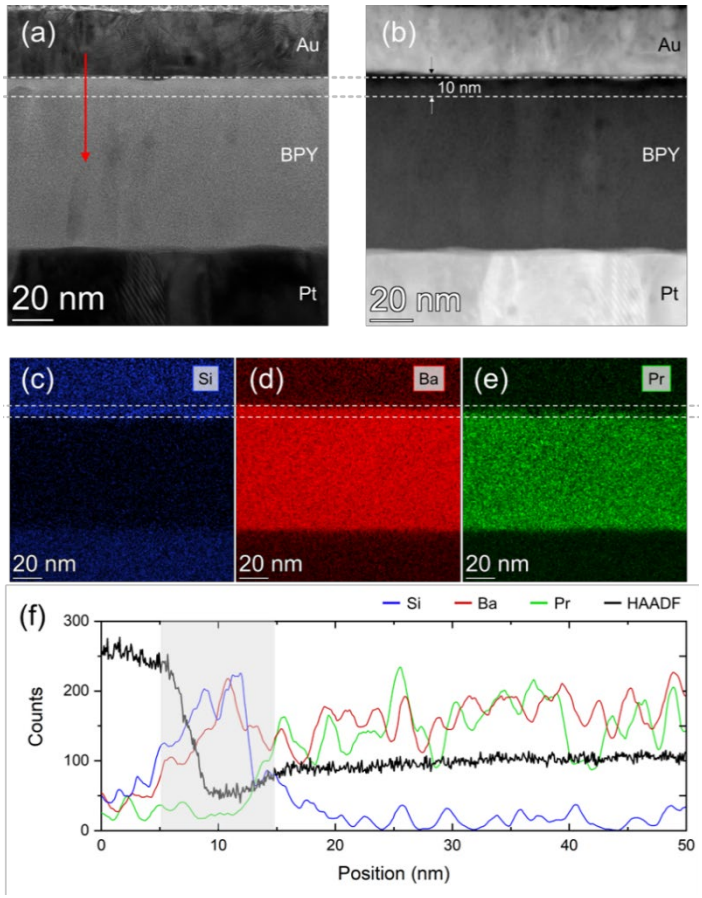

Figure 5 Bright field TEM micrograph (a) and HAADF STEM micrograph (b) of BPY thin film cross section after OTR/ECR measurements. Red arrow indicates the line scan position shown in (f). EDS mapping of Si (c), Ba (d), and Pr (e). The white dashed lines show the ~10 nm thick surface region with Si contamination.

We prepared multiple BCFZY thin film samples and FIB cross sections for S/TEM-EDS measurements under comparable conditions to those of the BPY film, in the optical furnace equipped with quartz tube and steam switching. (The corresponding OTR curve of the particular BCFZY thin film shown here for STEM-

EDS measurements is given in Figure S14.) From the bright field BCFZY micrograph, shown in **Figure 6(a)**, we observed a dense, monolithic film (~260 nm) comprising 20 nm-wide, columnar grains. Unlike for BPY, the cation distribution is uniform through the thickness of the film, shown in **Figure 6(c)-(e)**. Using the EDS K_α lines for quantification, the A- to B-site ratio ([Ba]:[Co+Fe+Zr+Y]) at the surface is nominally 0.75:1, with the same cation ratio preserved within the bulk of the film. The most pronounced difference between the BPY and BCFZY thin films seen with electron microscopy techniques after processing was the surface composition. The EDS spectra around the Si K_α peak (1.739 keV) for surface and bulk regions in BPY and BCFZY are shown in **Figure 7(a),(b)**, respectively. In **Figure 7(a)**, the BPY surface showed a large Si signal at the surface which is not present within the bulk of the film. However, the BCFZY film did not reveal any evidence of Si poisoning or Ba segregation by STEM-EDS.

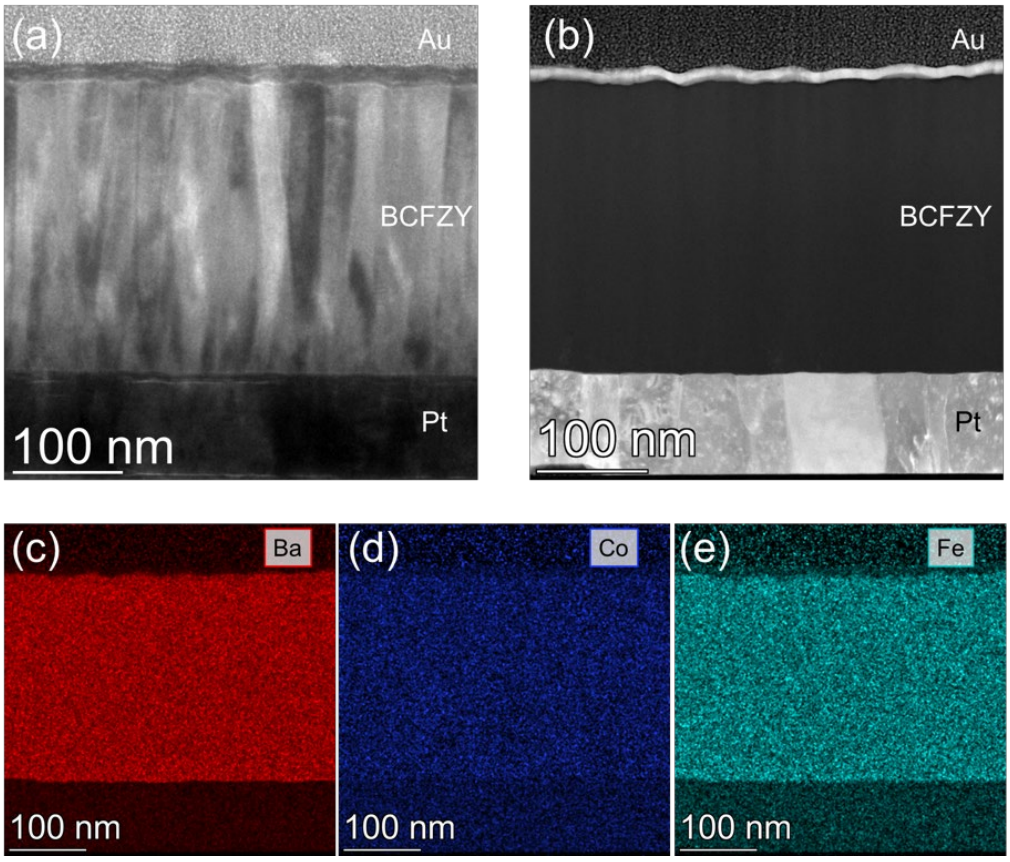

Figure 6 Bright field TEM micrograph (a) and HAADF STEM micrograph (b) of BCFZY thin film cross section. EDS mapping of Ba (c), Co (d), and Fe (e).

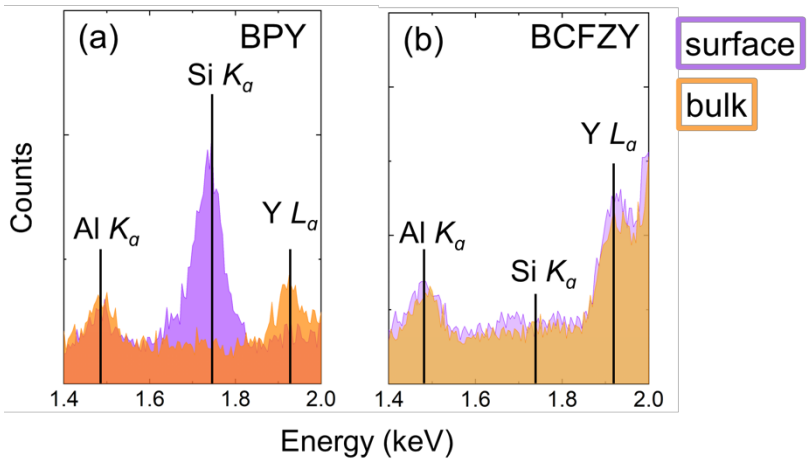

Figure 7 EDS spectra around the Si K_α peak for BPY (a) and BCFZY (b) thin films. The purple spectrum is representative of the surface layer (~10 nm) and the orange spectrum is from the bulk of the film – away from the surface and film-Pt interface.

Next, we performed angle-resolved XPS analyses on BCFZY and BPY films before vs. after relaxation measurements to identify the surface composition and its evolution, as shown in **Figure 8**. Angle-resolved XPS is a useful composition analysis technique which enables variation of the information depth by modulating the X-ray emission angles. [39] (A schematic of the angle-resolved XPS geometry is provided in Figure S15.) The XPS compositional analyses were performed at X-ray take-off angles (θ) of 90 and 30˚. When the X-ray take-off angle is 30˚ in XPS measurements, the detection depth is around ~1 nm theoretically, whereas for a take-off angle of 90° the information depth is closer to ~6 nm. (For the detection depth depending on elements, see Table S1.)

The high-resolution XPS spectra of Y 3*d*, Si 2*s*, and C 1*s* for the BPY and BCFZY thin films were measured at θ = 30˚, as shown in **Figure 8**. (For the XPS spectra of Y 3*d* and Si 2*s* at θ = 90˚, see Figure S16.) In **Figure 8(a)**, the XPS spectra of Y 3*d* were fitted with two peaks corresponding to Y $3d_{3/2}$ and Y $3d_{5/2}$ in the as-grown BPY thin film. However, after relaxation measurements, the XPS spectra revealed the presence of Si in addition to Y on the BPY thin film. The XPS spectra of C 1*s* also implied the presence of Si, considering the appearance of a shoulder attributed to a C-Si peak after OTR/ECR, as shown in **Figure 8(b)**. [40] In the case of the BCFZY thin film, the XPS spectra also included both the Si 2*s* and Y 3*d* peaks, similar to the BPY thin film. On the other hand, there was no evidence of a C-Si peak in the C 1*s* spectrum before or after relaxation measurements for BCFZY, as shown in **Figure 8(d)**. For BCFZY, this partial XPS evidence of surface Si appears inconsistent with its absence by STEM-EDS. It might be due to greater

sensitivity by XPS, or uneven Si contamination at the BCFZY thin film surface. We note that several BCFZY replicate films (post-ECR/OTR) and different positions on the films were examined by STEM-EDS, none of which revealed the presence of Si, and all of which demonstrated the absence of Ba segregation, unlike for the BPY film.

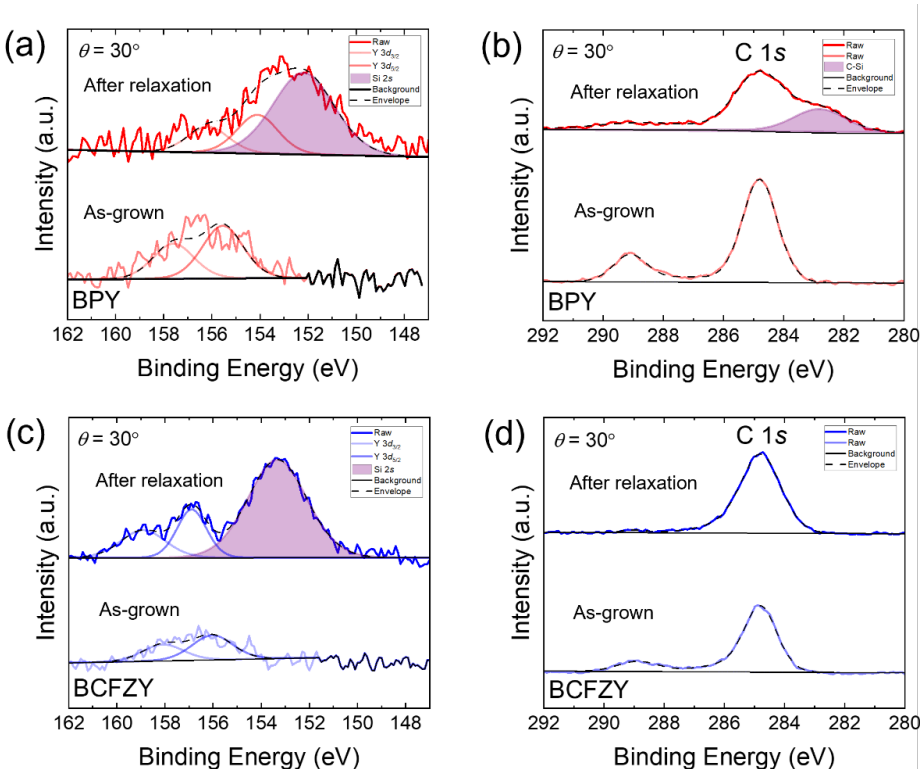

Figure 8 (a) XPS spectra of Y 3*d*, Si 2*s*, and C 1*s* for the BPY and BCFZY thin films, at a take-off angle (θ) of 30˚ before and after relaxation measurements.

To further assess the surface compositional changes of both thin films, all elemental XPS spectra were analyzed in terms of intensities. **Figure 9(a)-(d)** shows XPS spectra of Ba 3*d* specifically, for the BPY and BCFZY thin films at take-off angles of 30 and 90˚ before vs. after relaxation measurements, while XPS spectra pertaining to the other elements are provided in Figure S17. For BPY, the more surface-sensitive (θ = 30˚) Ba 3*d* spectra intensities decreased after relaxation measurements vs. the as-grown condition as shown in **Figure 9(a)**, while the data drawing from slightly deeper in the film at θ = 90˚ were almost constant before vs. after relaxation measurements, as shown in **Figure 9(c)**. These results are consistent with Si contamination (deposition) on the film surface during the relaxation measurements in the quartz tube in humid environments, which lessens the Ba signal (and all the film elements' signals) from the top ~ 0.3 nm of the BPY thin film. For the BCFZY thin film, the Ba 3*d* spectra intensities reduced at both angles of θ = 30 and 90˚ after relaxation measurements, as shown in **Figure 9(b),(d)**. The XPS results

suggest that, similar to the case of BPY thin film, the Si deposition from the quartz tube under humid environments altered the surface chemistry of the BCFZY thin film. Additionally, the Ba 3*d* core spectra were shifted to higher binding energies after ECR/OTR, indicating possible oxidation of the BCFZY film and/or change in carrier concentration during its relaxation heat treatment. In support of this interpretation, Figure S13 shows that the primary film XRD peak for BCFZY shifted to a higher angle after ECR/OTR, suggestive of oxidation-induced out-of-plane lattice contraction, where oxidation likely corresponds to higher hole concentration via electroneutrality considerations. This shift was not observed for the BPY film before vs. after ECR/OTR.

Analysis of surface compositions was attempted from XPS spectra for comparison to results from the other methods in this work. For BCFZY, an overlap of Ba 3*d* and Co 2*p* XPS spectra hindered quantitative compositional analysis. [23] However, the surface composition of the BPY film was quantified by fitting its XPS spectra as shown in **Figure 9(e),(f)**, using sensitivity factors for each element for this particular XPS instrument. The calculated Ba/(Pr+Y) ratio at a take-off angle of 30˚ was ~2.01 and ~ 2.48 before and after relaxation measurement, respectively. The calculated Ba/(Pr+Y) ratio at a take-off angle of 90˚ was ~ 2.11 and ~ 3.28 before and after relaxation measurement, respectively. It is evident that the Ba/(Pr+Y) ratio after relaxation measurement is higher than that of as-grown BPY thin film. Considering a nominal Ba/(Pr+Y) ratio of 1 in the bulk of BPY (as supported to some extent by other methods), the XPS results demonstrate a clear surface Ba enrichment relative to (Pr+Y) in the as-grown BPY film, which is further enhanced after the relaxation measurements. This result is consistent with the observed Ba-enrichment and Pr/Y deficiency at the surface of the BPY film after relaxation by STEM-EDS.

Comparisons of bulk and surface compositional analyses resulting from various methods in this work (XRF, RBS, XPS, STEM-EDS) for both the films and the ceramic PLD targets are given in **Tables 2-3**. Taken together, the results indicated that the BPY film was more Ba-rich than the BCFZY film, and that this higher overall A-site Ba concentration coincided with Ba excess on the surface. By contrast, STEM-EDS demonstrated that the Ba deficiency observed throughout the BCFZY film extended to the surface. Since the Ba-deficient BCFZY film exhibited a lower and less stable proton exchange *k* value, we pursued fabrication of a more stoichiometric BCFZY film. As shown in **Table 3**, a film grown later from the BCFZY target that had become Ba-enriched and at 20 Hz rather than the typical 5 Hz resulted in a higher Ba content in the film, as analysed by RBS (**Figure 10**). The corresponding *k* values were higher than those of the Ba-deficient BCFZY, as shown in **Figure 3**.

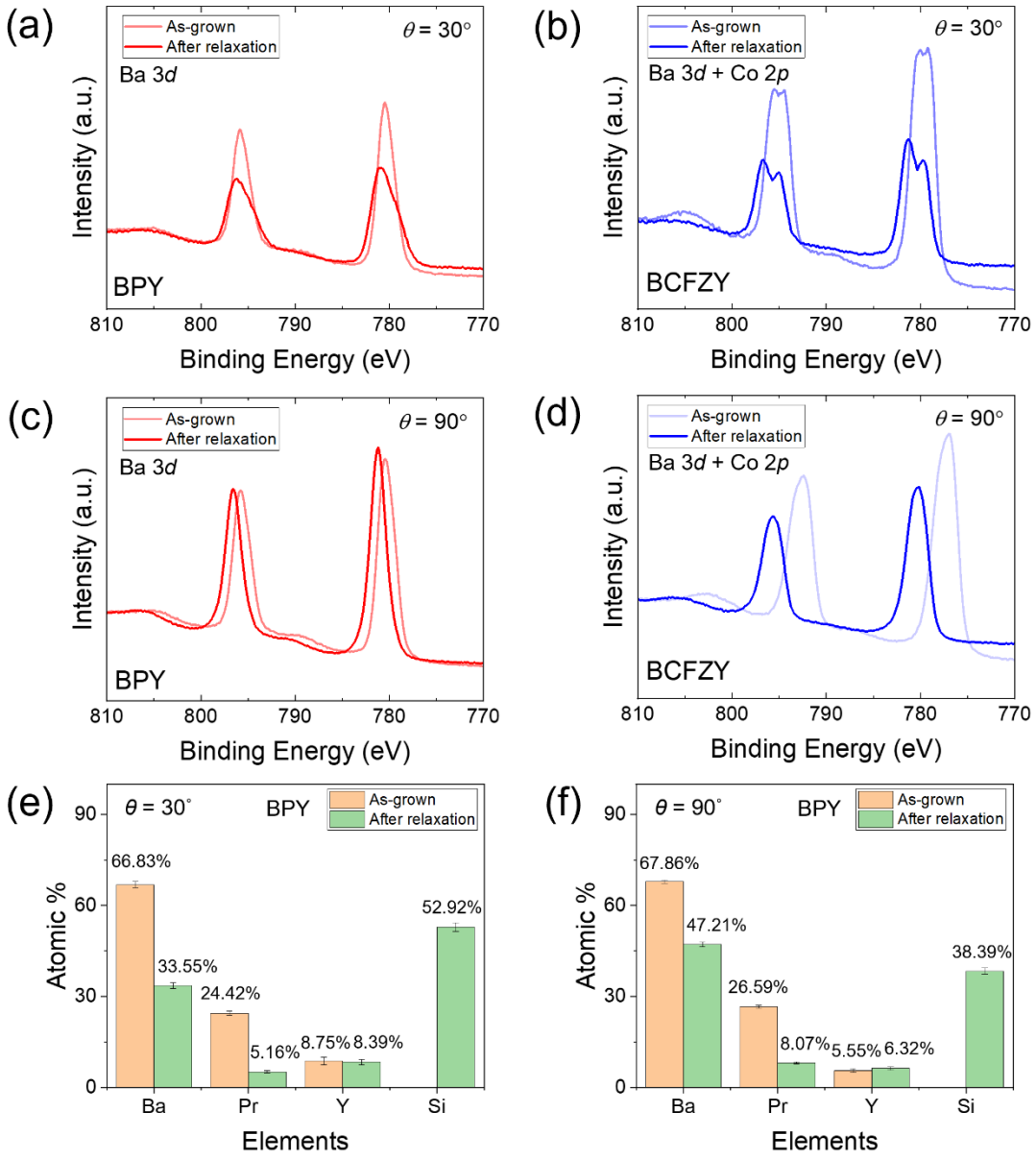

Figure 9 Ba 3*d* XPS spectra for the BPY (a),(c) and BCFZY (b),(d) thin films at take-off angles of $\theta = 30^{\circ}$ and 90˚, before vs. after relaxation measurements. Comparison of surface atomic percentages analyzed from XPS spectra fitting for the BPY thin film at take-off angles of θ = 30 (e) and 90˚ (f) before and after relaxation measurements.

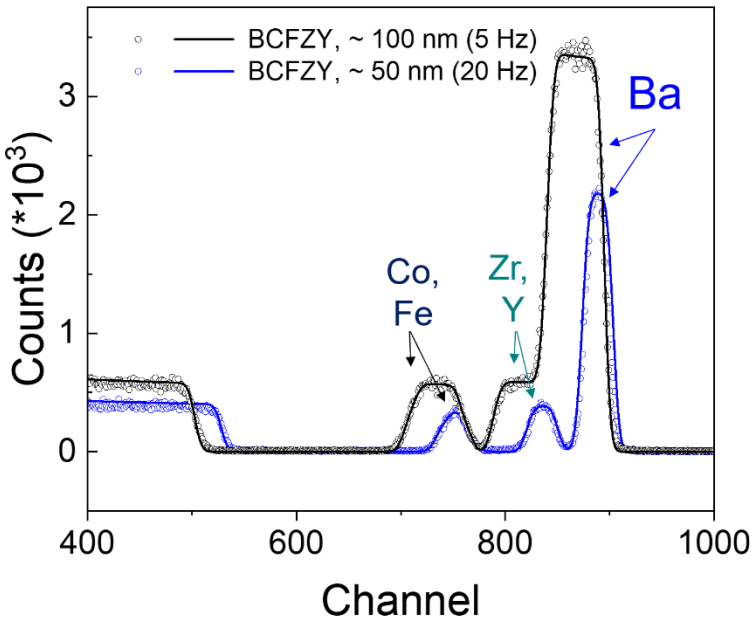

Figure 10 Rutherford backscattering spectrometry results and fitted lines of BCFZY thin films grown using an as-synthesized PLD target (at a repetition rate of 5 Hz) and a Ba-surface-enriched target after 1 year of PLD laser ablation (at a repetition rate of 20 Hz).

Table 2 Comparison of BPY thin film compositions.

$BaPr_{0.9}Y_{0.1}O_{3-\delta}$		**Ba**	**Pr**	**Y**	Si	**Ba/(Pr+Y) ratio**
Ideal atomic %		50%	45%	5%	0%	1
XRF PLD target atomic % (As synthesized) (± 0.5%)		52.01%	44.15%	3.84%	0%	1.08
(After ~ 1 year) (± 0.5%)		51.70%	44.45%	3.85%	0%	1.07
RBS thin film atomic % (± 1%) (*For the RBS spectra, Figure S18)	Before relaxation	58.75%	35.93%	5.32%	0%	1.42
			B-site: 41.25%			
XPS ($\theta = 90^{\circ}$) (± 2%)	Before relaxation	67.86%	26.59%	5.55%	0%	2.11
	After relaxation	**47.21%**	**8.07%**	**6.32%**	**38.39%**	**3.28**
XPS ($\theta = 30^{\circ}$) (± 2%)	Before relaxation	66.83%	24.42%	8.75%	0%	2.01
	After relaxation	**33.55%**	**5.16%**	**8.39%**	**52.92%**	**2.48**
STEM-EDS (Bulk) (± 2%)	**After relaxation**	**47%**	**41%**	**7%**	**5%**	**0.98**
STEM-EDS (Surface) (± 2%)	**After relaxation**	**44%**	**19%**	**4%**	**33%**	**1.91**

Table 3. Comparison of BCFZY thin film compositions.

$Ba(Co_{0.4}Fe_{0.4}Zr_{0.1}Y_{0.1})O_{3-\delta}$		**Ba**	**Co**	**Fe**	**Zr**	**Y**	**A/B ratio**
Ideal atomic %		50%	20%	20%	10%	10%	1
XRF PLD target atomic % (As synthesized) (± 0.5%)		46.86%	24.39%	16.47%	7.91%	4.38%	0.88
(After ~ 1 year) (± 0.5%)		64.95%	14.38%	9.22%	7.47%	3.98%	1.85
RBS thin film atomic % (5 Hz laser rep rate) (± 1%)	Before relaxation	47.4%	13.78%	22.26%	9.81%	6.75%	0.90
			B-site: 52.6%				
RBS thin film atomic % (20 Hz laser rep rate) (± 1%)	Before relaxation	49.6%	11.8%	23.1%	7.99%	7.51%	0.98
			B-site: 50.4%				
*20 Hz BCFZY thin film was grown from the BCFZY target with surface Ba-enrichment (confirmed by XRF) after approximately one year of laser ablation in the PLD system.							
XPS (Surface)	Before relaxation	Ba & Co spectra overlap					
	After relaxation						
XPS (More surface sensitive)	Before relaxation						
	After relaxation						
STEM-EDS (Bulk) (± 2%)	After relaxation	42%	13%	24%	14%	7%	0.72
STEM-EDS (Surface) (± 2%)	**After relaxation**	**42%**	**13%**	**24%**	**14%**	**7%**	**0.72**

4. Discussion

4.1. Reaction taking place

The application of simultaneous OTR and ECR provided insight into the nature of the material response to H_2O introduction. Typically, under intermediate-to-high pO_2 conditions, proton conductors can respond to an increase in pH_2O with hydration or hydrogenation (Eqs. 2-3), with the ratio of oxygen vacancy concentration to hole concentration influencing which response may dominate. [8] If hydration takes place, the proton concentration increases and oxygen vacancies are filled. If hydrogenation takes place, holes are consumed while protons are added. These two different ways to change the defect chemistry are expected to have distinct and distinguishable consequences for the optical and electrical behavior. In the present work, the decrease of the predominantly p-type conductivity and increase of optical transmission upon H_2O introduction is consistent with the lowering of hole concentration, as expected with hydrogenation. (By contrast, pure hydration would be expected to increase conductivity and cause little optical change at this wavelength.) We have shown previously that for MIECs, the optical absorption change can be proportional to the change in hole concentration. [19,21,41] In future work, DFT simulations of electronic structure and optical absorption changes in response to simulated hydration vs. hydrogenation processes (associated defect concentration changes) may be beneficial for more direct insight into the responses and identification of the most optimal probe wavelength to use (here ~2.8 eV worked well, but it may not be the most sensitive to hole concentration). For the most part, considering lower-temperature data that were not gas-flush-time-limited, the transient response took the form of an exponential function, consistent with the expectation of surface exchange-limited kinetics for this model geometry and enabling determination of the proton exchange *k* value.

4.2. Relationship between bulk composition, surface composition, and proton exchange kinetics

It is important to build up an understanding of how electrode composition impacts the proton exchange *k* values, performance stability, and the related surface chemistry evolution. By comparing BPY, Ba-deficient BCFZY, and more stoichiometric BCFZY we can contribute some initial inferences about the roles of A- and B-site cations. Considering the A-site, we observed a correlation between the proton-exchange *k* values, the overall A:B ratio, and the surface A:B ratio. Higher overall A-site concentrations promoted A-site enriched surfaces and were favorable for high *k* values, with good steam-splitting performance stability in the case of BPY. Comparing compositions summarized in **Table 2**, it is evident that the surface [Ba]/[Pr+Y] concentration ratio was above 1 in the as-grown BPY thin film, and it increased even further as a result of performing the relaxation measurements at 400-500 °C. On the other hand, the Ba deficiency in the initial BCFZY thin film (bulk and surface) correlated to poorer *k* and stability over time. The non-stoichiometric

BCFZY thin film with the lowest *k* values exhibited a [Ba]/[Co+Fe+Zr+Y] ratio as low as 0.72-0.9 according to S/TEM-EDS and RBS in **Table 3**, after relaxation measurements. To test the possible role of Ba concentration, we deposited BCFZY thin films using a Ba-enriched BCFZY target (also at a laser repetition rate of 20 Hz vs. the initial 5 Hz), leading to a recovery of the overall [Ba]/[Co+Fe+Zr+Y] ratio in the film from 0.9 to 0.98 (from RBS spectra, **Figure 10** and **Table 3**). The more stoichiometric BCFZY thin film with the increased overall A-site concentration showed faster *k* values upon steam switching compared to the non-stoichiometric BCFZY thin film, as shown in **Figure 3**. (For the corresponding OTR/ECR curves, see the Figure S19.) Therefore, it seems that a high A-site cation concentration boosts steam-splitting kinetics at intermediate temperatures. This finding stands in contrast to the A-site compositional strategy employed in preparation of established oxygen electrodes for solid oxide cells, where oxygen surface exchange (typically pure redox rather than redox plus hydration in the present work) takes place. There, A-site Ba/Sr surface segregation is considered to be a significant cause of performance deterioration, and compositions are often prepared intentionally A-site deficient to lessen the segregation tendency and thereby inhibit degradation [42–45]. A-site rich surface layers might hinder both electronic charge transfer and oxide ion transfer in that case. In the present work, perhaps the basicity conferred by the A-site cation is a more important contributor to the fast proton surface exchange, since that feature supports proton uptake. However, taken to the extreme, one might expect severe A-site segregation to form an electronically poor surface coating, which may hinder electronic charge transfer and possibly then favor hydration over hydrogenation, assuming protons can still transfer.

The basicity of the A-site cation-enriched surface also appears to promote reaction with acidic impurities, such as SiO_x from the gas phase, in the present work. Under humid conditions, volatile SiO_x or SiO_xH_y may form inside the quartz measurement tube, leading to Si deposition via vapor phase transport from the quartz tube onto the film surface. [25,46,47] Si is also a common impurity to consider for its potential presence in actual PCEC operation. For the mixed-conducting, fluorite-structured solid oxide cell electrode $Pr_{0.1}Ce_{0.9}O_{2-\delta}$ [25], Si is well known as a surface impurity that can degrade the oxygen exchange ability. [47] However, when it comes to perovskite (rather than fluorite) surface exchange performance in the presence of Si and to steam-splitting (rather than nominally dry oxygen exchange), little is known about the role of Si. In the present study, BPY exhibited a relatively thick (~ 10 nm by STEM-EDS) layer rich in Ba and Si after relaxation measurements, whereas Ba-deficient BCFZY did not. Despite formation of that Si-rich reaction phase, the BPY exhibited relatively stable and high proton-exchange *k* values over time, in contrast to the unstable BCFZY, which was unable to complete even 5 relaxations upon steam-switching. The exact structure of the surface layer on BPY is not fully known. From **Figure 8**, considering the XPS peak positions in the Si 2*s* and C 1*s* spectra, Si might form bonds such as Si-O-Si, Ba-O-Si, Pr-O-Si, Si-C, and/or Si-OH

at the BPY thin film surface. STEM-EDS indicates the surface layer has a cation composition of 44 at% Ba, 19 at% Pr, 4 at% Y, and 33 at% Si.

Considering the B-site, we observed that replacement of transition metal Co, Fe, and Zr with lanthanide Pr, upon going from BCFZY to BPY, did not harm the steam-splitting kinetics. Pr in $BaPrO_{3-\delta}$ films reportedly maintains multivalency and p-type conductivity at least under dry conditions, [33] which is likely essential for hydrogenation. Additionally, the lower electronegativity of Pr vs. Fe, Co, and Zr may promote greater basicity of the oxide ion and thus more favorable hydration thermodynamics. The larger size of Pr vs. Fe, Co, and Zr lowers the crystal symmetry and thus the B-O-B angles in the perovskite, with potential consequences for B-O bond charge distribution, which also may impact hydration thermodynamics. The B-site average ionic radius in BCFZY is approximately 71.9 pm (assuming high-spin Fe and Co in 3+ valence states, Y^{3+}, and Zr^{4+} in VI-fold coordination), and in BPY it is approximately 87.5 pm (assuming primarily Pr^{4+} and Y^{3+} in VI-fold coordination), yielding tolerance factors of ~1.00 and ~0.94, respectively. Correspondingly BCFZY has been reported as cubic [48] whereas the BPY exhibits a rhombohedral structure at intermediate temperatures (e.g., 400-700 ˚C) [49]. It seems possible that Pr also contributes to the stability of BPY despite being partially depleted at the surface, because both Ba-deficient and Ba-stoichiometric BCFZY films exhibited stability problems during relaxation studies. In other words, the A-site cation may not be the only or primary determiner of the long-term stability in the presence of humidity and at intermediate temperatures.

4.3. Further Insight into Surface Chemistry Evolution of BPY from Y 3*d* and Ba 3*d* X-ray Photoelectron Spectra

From analysis of XPS peak positions including splitting, comparing different take-off angles and pre- vs. post- steam relaxation testing results, one can in principle gain further insight into depth-dependent evolution of local chemical environment. In this part of the discussion, we suggest some possible interpretations of the BPY films' Y 3*d* and Ba 3*d* peak positions, noting some uncertainty due to the close convolution of "surface" vs "lattice" contributions in some cases and any potential charging effects.

Y 3d.: Although the there is some peak overlap, we fitted and summarized the peak positions of the Y 3*d* spectra using two doublets to deconvolute the surface and lattice Y species in the BPY thin films at $\theta = 30$ and 90˚ as shown in **Table S2** and **Figure S20**. First, the lower-binding-energy Y 3*d* peak positions (Y $3d_{3/2}$ at 156.7~156.8 eV of and Y $3d_{5/2}$ at 154.7~154.8 eV) in the BPY thin film are reasonably consistent (+/- 0.5 eV) with the peak positions (Y $3d_{3/2}$ at 157.2 eV and Y $3d_{5/2}$ at 155.1 eV) of lattice Y'_{Zr} in Y doped $BaZrO_3$ in the literature [50]. This agreement suggests that Y substituted on the Pr site in the 6-fold-coordinated perovskite B-site, as expected. Note that the charging effect can slightly shift the peak positions

to higher binding energies. [51] Second, the other peak pairs (Y $3d_{3/2}$ at 158.4~158.8 eV and Y $3d_{5/2}$ at 156.4~156.8 eV) featured a positive shift of binding energy, which implies the Y bonds to a more electronegative group [e.g., hydroxide $Y(OH)_3$, carbonate $Y(CO_3)_3$, hydroxycarbonate $Y_2(OH)_x(CO_3)_y$, oxycarbonate $Y_2O_x(CO_3)_y$], suggesting that they correspond to possible surface yttrium compounds when the samples are exposed to the ambient air. Among them, the yttrium hydroxide might be a possible surface secondary phase in the as-grown BPY thin film because the peak positions (Y $3d_{3/2}$ of 158.4 eV and Y $3d_{5/2}$ of 156.4 eV) are closer to those of yttrium hydroxide (Y $3d_{3/2}$ at 158.5 eV and Y $3d_{5/2}$ at 156.5 eV) from $BaCe_xZr_{0.9-x}Y_{0.1}O_{2.95}$ in the literature. [50] After steam exposure/relaxation, one Y 3*d* doublet overlaps with the Si 2*s* peak. It is therefore challenging to deconvolute the XPS spectra, to determine the contributions from lattice Y or surface Y. Nevertheless, after intermediate-temperature steam relaxation testing, at θ = 30˚ (more surface-sensitive) the peaks attributed to lattice and surface Y are shifted to lower binding energies, with a decrease of 0.6 and 2.3 eV, respectively, as shown in **Figure S20**. On the other hand at θ = 90˚ (deeper information depth), the binding energy of lattice Y is increased by 1.4 eV after heating and steam relaxations. It indicates that the heating plus steam exposure/relaxation transformed the Y coordination environment differently depending on its depth. The negative and positive chemical shifts relative to the as-grown state might indicate growth of surface secondary phases such as surface yttrium hydroxide and oxidation in the bulk, respectively. [52] Meanwhile, the heating and steam exposure increases surface roughness from 0.57 to 6.68 nm. This change might also be due to larger grains of adsorbed hydroxides at the BPY thin film surface. Grain size / surface roughness typically increases with film annealing even in the absence of hydroxides however. Moreover, the main difference between before and after steam exposure/relaxation in the BPY thin film is the emergence of Si 2*s* spectra by formation of Si-related compounds, so the larger grains may reflect those species.

Ba 3d: For the quantitative analyses of XPS Ba 3*d* and O 1*s* spectra, we performed all the data fitting and report peak positions of Ba $3d_{3/2}$ and Ba $3d_{5/2}$ in **Table S2** and **Figure S21**. The peaks at higher binding energy (blue lines) of the Ba 3*d* spectra are characteristic of the surface sensitive environment, whereas the peaks at lower binding energy (red lines) are characteristic of the lattice environment. [53] The area ratio of the surface:bulk fitted Ba $3d_{5/2}$ spectra is 0.174 at θ = 30˚ and 0.112 at θ = 90˚, in the as-grown BPY thin film, in **Table S3**. The as-grown BPY thin film already contains some surface Ba in an environment different to that of the bulk Ba, e.g. Ba hydroxide or under-coordinated Ba-O units. [52] After steam relaxation, the surface:bulk area ratios of the fitted Ba $3d_{5/2}$ spectra are 1.367 and ∞ at θ = 30 and 90˚, respectively, in the BPY thin film in **Table S3**. In other words, the surface Ba signal increased considerably in intensity after steam-relaxation testing, which is consistent with the observed Ba-enriched surface seen more clearly by STEM-EDS measurements. Also, we fitted O 1*s* spectra to deconvolute the components as shown in **Figure S22**. At the O 1*s* spectra measured at θ = 30˚ in the BPY thin film after steam relaxation, we observed the

unusual peak of 527.7 eV, which is closer to that of BaO in the literature. [54] This result is also consistent with Ba-enrichment/segregation at the BPY surface after steam relaxation.

4.4. Impact of substrate

Observed proton exchange *k* values were generally slightly higher for films grown on MgO vs. those grown on Al_2O_3. A comprehensive investigation of the possible reasons is beyond the scope of this work, but we note that both substrates individually were confirmed to be inert in terms of electrical and optical responses to introduction of H_2O at 400-500 °C, unlike certain perovskite substrate compositions tested in isolation (e.g. $SrTiO_3$). The relationship of the substrate lattice parameter and symmetry to those of the film can influence the crystallographic orientation/ degree of texture, microstructure, and crystalline quality of films, all of which may in principle impact the *k* values. Further, strain, whether from coherent matching to substrates, growth-induced stress [55], and/or stoichiometry variations [56] could play a role in the *k* values. Compared to hexagonal sapphire, the cubic MgO substrate has both better lattice parameter matching to the films (~2.6% mismatch vs. BCFZY at 4.10 Å [12] and ~4.0% mismatch vs. BPY at 4.38 Å [49]) and closer coefficient of thermal expansion ($1.26*10^{-5}$ K^{-1} [41] for MgO, $2.16*10^{-5}$ K^{-1} [12] for BCFZY, and $1.31*10^{-5}$ K^{-1} for BPY ($R\bar{3}c$) [34] vs. $7.3*10^{-6}$ K^{-1} [57] along sapphire *a*-axis). On this basis, one expects potentially better crystalline quality for the films grown on MgO with the possibility for substrate-induced strain. A comparison of XRD patterns and AFM images in **Figure 1** and **Figure S3** reveals however only slight differences in films' structures, as deposited, depending on substrate. Within the limited data set of 4 films, there is no systematic impact of substrate on grain size or RMS roughness of the films, as-deposited: the grain size appears larger for BPY on MgO and smaller for BCFZY on MgO relative to the films on sapphire, but the differences are small. The out-of-plane orientations of the films are also not varying with substrate. For the BCFZY films, the strong (110) reflection of the film grown on MgO is positioned at a higher angle than that of the film grown on sapphire, where the reflection is less intense. Its smaller out-of-plane lattice parameter might imply that the film grown on MgO was more oxidized or less hydrated at that time. On the other hand, for the BPY films, the (121) peak of the film grown on MgO is positioned at a slightly lower angle than that of film grown on sapphire, suggesting perhaps slightly higher reduction or hydration at that point. Regardless, the degree of oxidation and hydration is expected to change during the elevated-temperature testing in steam, so these small differences as-deposited may not be significant for the measured *k* values. One possibility may be that different ions/impurities from the two substrate chemistries diffuse up through the films' grain boundaries to the surfaces causing slight changes in *k* values as a function of substrate; we did not specifically observe trace impurities beyond Si by XPS or STEM-EDS in this work, however.

5. Conclusion

In this work, we fabricated and compared two perovskite triple conducting oxides by growing geometrically well-defined films of BPY and BCFZY with PLD. We examined the proton exchange *k*-values using simultaneous *in-situ* optical transmission relaxation and electrical conductivity relaxation measurements upon switching pH_2O at ~ 400 and 500 ˚C, and continued these switches as a function of time to assess stability. To our knowledge, this is the first use of an optical transmission method to probe elevated temperature steam splitting kinetics, and we interpreted the optical (and electrical) changes as indicative of reduction/oxidation during the hydrogenation/dehydrogenation process. The *k* values of BPY thin films were generally higher than those of the BCFZY thin films grown under identical conditions, and BPY also retained higher *k* values over time, demonstrating greater performance stability. Counter to the observed surface exchange behavior, the BPY film demonstrated the largest changes in surface composition and morphology after vs. before OTR/ECR. The BPY film as a whole was close to the ideal stoichiometry as-deposited, perhaps slightly A-site rich (depending on analysis method); relatedly, its surface was Ba-enriched as-grown, and this Ba enrichment increased as a result of the ECR/OTR testing. STEM-EDS revealed a significant Si concentration in the Ba-enriched surface region after ECR/OTR. For BCFZY, the films grown under the same condition were Ba-deficient overall, leading to no obvious Ba surface segregation, and a suppressed reaction with Si at the surface. Given the better performance of Ba-surface-rich BPY for steam-splitting, we prepared BCFZY with a higher Ba content, and these films exhibited improved proton exchange *k* values vs. the Ba-deficient BCFZY. We conclude that, in contrast to SOEC electrodes where A-site Ba/Sr enrichment is thought to be avoided for fast oxygen surface exchange, PCEC electrodes' proton exchange kinetics are benefitted by a basic Ba-rich surface, even though it reacts with acidic impurities. Further, replacement of the nominally multivalent transition metal elements (Fe, Co) with lanthanide (Pr) on the B-site did not prevent hydrogenation from taking place well. Our work offers a beneficial approach, leveraging geometrically well-defined thin films and continuous OTR/ECR, to quantify proton exchange *k* values and their stability on emerging triple conductor compositions. Additionally, we suggest the BPY composition as a simpler, Co-free, potentially more efficient and stable alternative to the benchmark BCFZY anode.

Author Contributions

JL: Formal analysis, investigation, methodology, visualization, writing- original draft

HBB: Formal analysis, investigation, writing- original draft

NHP: Conceptualization, funding acquisition, methodology, project administration, resources, supervision (JL, HBB), writing- review & editing

Conflicts of Interest

There are no conflicts of interest to declare.

Acknowledgements

The authors would like to acknowledge the primary funding from bp through the bp International Centre for Advanced Materials (bp-ICAM) through project ICAM76. HBB and NHP also acknowledge support from the Department of Energy, Basic Energy Sciences through grant DE-SC0018963. The RBS, XRD, AFM, S/TEM-EDS, and angle-resolved XPS measurements were carried out in the Illinois Materials Research Laboratory Central Research Facilities, University of Illinois. The authors acknowledge the use of facilities and instrumentation supported by NSF through the University of Illinois Materials Research Science and Engineering Center DMR-1720633.

References

(1) Merkle, R. Proton and Mixed Proton/Hole-Conducting Materials for Protonic Ceramic Electrolysis Cells. In *High-Temperature Electrolysis*; IOP Publishing, 2023; pp 11–1. https://doi.org/10.1088/978-0-7503-3951-3ch11.

(2) Duan, C.; Huang, J.; Sullivan, N.; O'Hayre, R. Proton-Conducting Oxides for Energy Conversion and Storage. *Applied Physics Reviews* **2020**, *7* (1), 011314. https://doi.org/10.1063/1.5135319.

(3) Choi, S.; Kucharczyk, C. J.; Liang, Y.; Zhang, X.; Takeuchi, I.; Ji, H.-I.; Haile, S. M. Exceptional Power Density and Stability at Intermediate Temperatures in Protonic Ceramic Fuel Cells. *Nature Energy* **2018**, *3* (3), 202–210. https://doi.org/10.1038/s41560-017-0085-9.

(4) Ji, H.-I.; Lee, J.-H.; Son, J.-W.; Yoon, K. J.; Yang, S.; Kim, B.-K. Protonic Ceramic Electrolysis Cells for Fuel Production: A Brief Review. *Journal of the Korean Ceramic Society* **2020**, *57* (5), 480–494. https://doi.org/10.1007/s43207-020-00059-4.

(5) Vøllestad, E.; Strandbakke, R.; Tarach, M.; Catalán-Martínez, D.; Fontaine, M.-L.; Beeaff, D.; Clark, D. R.; Serra, J. M.; Norby, T. Mixed Proton and Electron Conducting Double Perovskite Anodes for Stable and Efficient Tubular Proton Ceramic Electrolysers. *Nature Materials* **2019**, *18* (7), 752–759. https://doi.org/10.1038/s41563-019-0388-2.

(6) Su, H.; Hu, Y. H. Degradation Issues and Stabilization Strategies of Protonic Ceramic Electrolysis Cells for Steam Electrolysis. *Energy Science & Engineering* **2022**, *10* (5), 1706–1725. https://doi.org/10.1002/ese3.1010.

(7) Bi, L.; Boulfrad, S.; Traversa, E. Steam Electrolysis by Solid Oxide Electrolysis Cells (SOECs) with Proton-Conducting Oxides. *Chem. Soc. Rev.* **2014**, *43* (24), 8255–8270. https://doi.org/10.1039/C4CS00194J.

(8) Merkle, R.; Hoedl, M. F.; Raimondi, G.; Zohourian, R.; Maier, J. Oxides with Mixed Protonic and Electronic Conductivity. *Annu. Rev. Mater. Res.* **2021**, *51* (1), 461–493. https://doi.org/10.1146/annurev-matsci-091819-010219.

(9) Kreuer, K. D. Proton-Conducting Oxides. *Annu. Rev. Mater. Res.* **2003**, *33* (1), 333–359. https://doi.org/10.1146/annurev.matsci.33.022802.091825.

(10) Papac, M.; Stevanović, V.; Zakutayev, A.; O'Hayre, R. Triple Ionic–Electronic Conducting Oxides for next-Generation Electrochemical Devices. *Nature Materials* **2021**, *20* (3), 301–313. https://doi.org/10.1038/s41563-020-00854-8.

(11) Shin, Y.; Kim, Y.; Sanders, M.; Harvey, S. P.; Walker, M.; O'Hayre, R. Tuning the Co/Fe Ratio in $BaCo_xFe_{0.8-x}Zr_{0.1}Y_{0.1}O_{3-\delta}$, a Promising Triple Ionic and Electronic Conducting Oxide, to Boost Electrolysis and Fuel Cell Performance. *J. Mater. Chem. A* **2022**, *10* (46), 24839–24853. https://doi.org/10.1039/D2TA03150G.

(12) Duan, C.; Hook, D.; Chen, Y.; Tong, J.; O'Hayre, R. Zr and Y Co-Doped Perovskite as a Stable, High Performance Cathode for Solid Oxide Fuel Cells Operating below 500 °C. *Energy Environ. Sci.* **2017**, *10* (1), 176–182. https://doi.org/10.1039/C6EE01915C.

(13) Chen, Y.; Hong, T.; Wang, P.; Brinkman, K.; Tong, J.; Cheng, J. Investigate the Proton Uptake Process of Proton/Oxygen Ion/Hole Triple Conductor $BaCo_{0.4}Fe_{0.4}Zr_{0.1}Y_{0.1}O_{3-\delta}$ by Electrical Conductivity Relaxation. *Journal of Power Sources* **2019**, *440*, 227122. https://doi.org/10.1016/j.jpowsour.2019.227122.

(14) Skubida, W.; Niemczyk, A.; Zheng, K.; Liu, X.; Świeczek, K. Crystal Structure, Hydration, and Two-Fold/Single-Fold Diffusion Kinetics in Proton-Conducting $Ba_{0.9}La_{0.1}Zr_{0.25}Sn_{0.25}In_{0.5}O_{3-a}$ Oxide. *Crystals* **2018**, *8* (3). https://doi.org/10.3390/cryst8030136.

(15) Ruf, M.; Solís, C.; Escolástico, S.; Dittmeyer, R.; Serra, J. M. Transport Properties and Oxidation and Hydration Kinetics of the Proton Conductor Mo Doped $Nd_{5.5}WO_{11.25-\delta}$. *J. Mater. Chem. A* **2014**, *2* (43), 18539–18546. https://doi.org/10.1039/C4TA03248A.

(16) Baumann, F. S.; Fleig, J.; Habermeier, H.-U.; Maier, J. Impedance Spectroscopic Study on Well-Defined $(La,Sr)(Co,Fe)O_{3-\delta}$ Model Electrodes. *Solid State Ionics* **2006**, *177* (11), 1071–1081. https://doi.org/10.1016/j.ssi.2006.02.045.

(17) Venkatesan, T. Pulsed Laser Deposition—Invention or Discovery? *Journal of Physics D: Applied Physics* **2013**, *47* (3), 034001. https://doi.org/10.1088/0022-3727/47/3/034001.

(18) Skiba, E. J.; Chen, T.; Perry, N. H. Simultaneous Electrical, Electrochemical, and Optical Relaxation Measurements of Oxygen Surface Exchange Coefficients: $Sr(Ti,Fe)O_{3-d}$ Film Crystallization Case Study. *ACS Appl. Mater. Interfaces* **2020**, *12* (43), 48614–48630. https://doi.org/10.1021/acsami.0c14265.

(19) Buckner, H. B.; Perry, N. H. In Situ Optical Absorption Studies of Point Defect Kinetics and Thermodynamics in Oxide Thin Films. *Advanced Materials Interfaces* **2019**, *6* (15), 1900496. https://doi.org/10.1002/admi.201900496.

(20) Skiba, E. J.; Perry, N. H. High-Temperature 2D Optical Relaxation Visualizes Enhanced Oxygen Exchange Kinetics at Metal-Mixed Conducting Oxide Interfaces. *ACS Appl. Mater. Interfaces* **2022**, *14* (42), 47659–47673. https://doi.org/10.1021/acsami.2c12184.

(21) Chen, T.; Harrington, G. F.; Masood, J.; Sasaki, K.; Perry, N. H. Emergence of Rapid Oxygen Surface Exchange Kinetics during in Situ Crystallization of Mixed Conducting Thin Film Oxides. *ACS Appl. Mater. Interfaces* **2019**, *11* (9), 9102–9116. https://doi.org/10.1021/acsami.8b21285.

(22) Ryu, S.; Lee, S.; Jeong, W.; Pandiyan, A.; Krishna Moorthy, S. B.; Chang, I.; Park, T.; Cha, S. W. Pulsed Laser Deposition of $BaCo_{0.4}Fe_{0.4}Zr_{0.1}Y_{0.1}O_{3-\delta}$ Cathode for Solid Oxide Fuel Cells. *Surface and Coatings Technology* **2019**, *369*, 265–268. https://doi.org/10.1016/j.surfcoat.2019.01.034.

(23) Pan, J.; Ye, Y.; Zhou, M.; Sun, X.; Chen, Y. Revealing the Impact of Steam Concentration on the Activity and Stability of Double-Perovskite Air Electrodes for Proton-Conducting Electrolysis Cells. *Energy Fuels* **2022**, *36* (19), 12253–12260. https://doi.org/10.1021/acs.energyfuels.2c02560.

(24) Chen, H.; Guo, Z.; Zhang, L. A.; Li, Y.; Li, F.; Zhang, Y.; Chen, Y.; Wang, X.; Yu, B.; Shi, J.; Liu, J.; Yang, C.; Cheng, S.; Chen, Y.; Liu, M. Improving the Electrocatalytic Activity and Durability of the $La_{0.6}Sr_{0.4}Co_{0.2}Fe_{0.8}O_{3-\delta}$ Cathode by Surface Modification. *ACS Appl. Mater. Interfaces* **2018**, *10* (46), 39785–39793. https://doi.org/10.1021/acsami.8b14693.

(25) Zhao, L.; Perry, N. H.; Daio, T.; Sasaki, K.; Bishop, S. R. Improving the Si Impurity Tolerance of $Pr_{0.1}Ce_{0.9}O_{2-\delta}$ SOFC Electrodes with Reactive Surface Additives. *Chem. Mater.* **2015**, *27* (8), 3065–3070. https://doi.org/10.1021/acs.chemmater.5b00501.

(26) Choi, S.; Davenport, T. C.; Haile, S. M. Protonic Ceramic Electrochemical Cells for Hydrogen Production and Electricity Generation: Exceptional Reversibility, Stability, and Demonstrated Faradaic Efficiency. *Energy Environ. Sci.* **2019**, *12* (1), 206–215. https://doi.org/10.1039/C8EE02865F.

(27) Ding, H.; Wu, W.; Jiang, C.; Ding, Y.; Bian, W.; Hu, B.; Singh, P.; Orme, C. J.; Wang, L.; Zhang, Y.; Ding, D. Self-Sustainable Protonic Ceramic Electrochemical Cells Using a Triple Conducting Electrode for Hydrogen and Power Production. *Nature Communications* **2020**, *11* (1), 1907. https://doi.org/10.1038/s41467-020-15677-z.

(28) Fukui, T.; Ohara, S.; Kawatsu, S. Conductivity of $BaPrO_3$ Based Perovskite Oxides. *Journal of Power Sources* **1998**, *71* (1), 164–168. https://doi.org/10.1016/S0378-7753(97)02813-9.

(29) Mimuro, S.; Shibako, S.; Oyama, Y. Kobayashi, K.; Higuchi, T.; Shin, S.; Yamaguchi, S. Proton incorporation and defect chemistry of Yb-doped $BaPrO_3$. *Solid State Ionics* **2007,** 178, 641-647. https://doi.org/10.1016/j.ssi.2007.02.006.

(30) Gorelov, V.P.; Kuzin, B.L.; Balakireva, V.B.; Sharova, N.V.; Vdovin, G.K.; Beresnev, S.M.; Kleshchev, Yu.N.; Brusentsov, V.P. Electroconductivity, Nature of Conduction, Thermodynamic Stability of the $BaPr_{1-x}Y_xO_{3-\alpha}$ Ceramics. Russian Journal of Electrochemistry **2001,** 37, 505–511. https://doi.org/10.1023/A:1016628205030

(31) Furuichi, S.; Tsuchiya, T.; Horiba, K.; Kobayashi, M.; Minohara, M.; Kumigashira, H.; Higuchi, T. Structural and Electrical Properties of $BaPrO_{3-\delta}$ Thin Film with Oxygen Vacancies. *Transactions of the Materials Research Society of Japan* **2017**, *42* (2), 15–18. https://doi.org/10.14723/tmrsj.42.15.

(32) Furuichi, S.; Tsuchiya, T.; Minohara, M.; Kobayashi, M.; Horiba, K.; Kumigashira, H.; Higuchi, T. Ion Conduction of $BaPrO_{3-\delta}$ Thin Film with Mixed Valence State for SOFC Anode Electrode. *ECS Trans.* **2017,** 75(42), 99-103. https://doi.org/10.1149/07542.0099ecst

(33) Jones, C. Y.; Wu, J.; Li, L.; Haile, S. M. Hydrogen Content in Doped and Undoped $BaPrO_3$ and $BaCeO_3$ by Cold Neutron Prompt-Gamma Activation Analysis. *Journal of Applied Physics* **2005**, *97* (11), 114908. https://doi.org/10.1063/1.1922590.

(34) Anderson, L. O.; Yong, A. X. B.; Ertekin, E.; Perry, N. H. Toward Zero-Strain Mixed Conductors: Anomalously Low Redox Coefficients of Chemical Expansion in Praseodymium-Oxide Perovskites. *Chem. Mater.* **2021**, *33* (21), 8378–8393. https://doi.org/10.1021/acs.chemmater.1c02739.

(35) Fairley, N.; Fernandez, V.; Richard-Plouet, M.; Guillot-Deudon, C.; Walton, J.; Smith, E.; Flahaut, D.; Greiner, M.; Biesinger, M.; Tougaard, S.; Morgan, D.; Baltrusaitis, J. Systematic and Collaborative Approach to Problem Solving Using X-Ray Photoelectron Spectroscopy. *Applied Surface Science Advances* **2021**, *5*, 100112. https://doi.org/10.1016/j.apsadv.2021.100112.

(36) *Carbon X-ray photoelectron spectra, carbon electron configuration, and other elemental information.* https://www.thermofisher.com/us/en/home/materials-science/learning-center/periodic-table/non-metal/carbon.html.

(37) Higuchi, T.; Oda, A.; Tsuchiya, T.; Suetsugu, T.; Suzuki, N.; Yamaguchi, S.; Minohara, M.; Kobayashi, M.; Horiba, K.; Kumigashira, H. Hole-Ion Mixed Conduction of Orientation-Controlled $BaPrO_{3-\delta}$ Thin Film with Mixed Valence States. *J. Phys. Soc. Jpn.* **2015**, *84* (11), 114708. https://doi.org/10.7566/JPSJ.84.114708.

(38) Seong, A.; Kim, J.; Jeong, D.; Sengodan, S.; Liu, M.; Choi, S.; Kim, G. Electrokinetic Proton Transport in Triple ($H^+/O^{2-}/e^-$) Conducting Oxides as a Key Descriptor for Highly Efficient Protonic Ceramic Fuel Cells. *Advanced Science* **2021**, *8* (11), 2004099. https://doi.org/10.1002/advs.202004099.

(39) Greczynski, G.; Hultman, L. A Step-by-Step Guide to Perform x-Ray Photoelectron Spectroscopy. *Journal of Applied Physics* **2022**, *132* (1), 011101. https://doi.org/10.1063/5.0086359.

(40) Bashouti, M. Y.; Paska, Y.; Puniredd, S. R.; Stelzner, T.; Christiansen, S.; Haick, H. Silicon Nanowires Terminated with Methyl Functionalities Exhibit Stronger Si–C Bonds than Equivalent 2D Surfaces. *Phys. Chem. Chem. Phys.* **2009**, *11* (20), 3845–3848. https://doi.org/10.1039/B820559K.

(41) Perry, N. H.; Kim, N.; Ertekin, E.; Tuller, H. L. Origins and Control of Optical Absorption in a Nondilute Oxide Solid Solution: $Sr(Ti,Fe)O_{3-x}$ Perovskite Case Study. *Chem. Mater.* **2019**, *31* (3), 1030–1041. https://doi.org/10.1021/acs.chemmater.8b04580.

(42) Koo, B.; Kim, K.; Kim, J. K.; Kwon, H.; Han, J. W.; Jung, W. Sr Segregation in Perovskite Oxides: Why It Happens and How It Exists. *Joule* **2018**, *2* (8), 1476–1499. https://doi.org/10.1016/j.joule.2018.07.016.

(43) Perry, N. H.; Ishihara, T. Roles of Bulk and Surface Chemistry in the Oxygen Exchange Kinetics and Related Properties of Mixed Conducting Perovskite Oxide Electrodes. *Materials* **2016**, *9* (10). https://doi.org/10.3390/ma9100858.

(44) Lee, W.; Yildiz, B. Factors That Influence Cation Segregation at the Surfaces of Perovskite Oxides. *ECS Transactions* **2013**, *57* (1), 2115. https://doi.org/10.1149/05701.2115ecst.

(45) Jin, T.; Lu, K. Surface and Interface Behaviors of (La0.8Sr0.2)XMnO3 Air Electrode for Solid Oxide Cells. *Journal of Power Sources* **2011**, *196* (20), 8331–8339. https://doi.org/10.1016/j.jpowsour.2011.06.052.

(46) Seo, H. G.; Staerz, A.; Kim, D. S.; LeBeau, J. M.; Tuller, H. L. Tuning Surface Acidity of Mixed Conducting Electrodes: Recovery of Si-Induced Degradation of Oxygen Exchange Rate and Area Specific Resistance. *Advanced Materials* **2022**, *n/a* (n/a), 2208182. https://doi.org/10.1002/adma.202208182.

(47) Staerz, A.; Seo, H. G.; Defferriere, T.; Tuller, H. L. Silica: Ubiquitous Poison of Metal Oxide Interfaces. *J. Mater. Chem. A* **2022**, *10* (6), 2618–2636. https://doi.org/10.1039/D1TA08469K.

(48) Duan, C.; Tong, J.; Shang, M.; Nikodemski, S.; Sanders, M.; Ricote, S.; Almansoori, A.; O'Hayre, R. Readily Processed Protonic Ceramic Fuel Cells with High Performance at Low Temperatures. *Science* **2015**, *349* (6254), 1321–1326.

(49) Knee, C. S.; Magrasó, A.; Norby, T.; Smith, R. I. Structural Transitions and Conductivity of $BaPrO_3$ and $BaPr_{0.9}Y_{0.1}O_{3-\delta}$. *J. Mater. Chem.* **2009**, *19* (20), 3238–3247. https://doi.org/10.1039/B820976F.

(50) Wang, Y.; Wang, L.; Chen, Y.; Hu, X.; Yu, Y.; Yang, N. Effect of Surface Defect Engineering on Proton Conductivity in Yttrium-Doped Barium Zirconate Thin Films. *J. Phys. Chem. C* **2023**, *127* (19), 8937–8945.

(51) https://www.xpsfitting.com/2012/08/charge-compensation.html

(52) Jarry, A.; Ricote, S.; Geller, A.; Pellegrinelli, C.; Zhang, X.; Stewart, D.; Takeuchi, I.; Wachsman, E.; Crumlin, E. J.; Eichhorn, B. *ACS Appl. Mater. Interfaces* **2018**, *10*, 37661−37670.

(53) Agudelo-Estrada, S.; Barrett, N.; Lubin, C.; Wolfman, J.; Negulescu, B.; Andreazza, P.; Ruyter, A. *EPJ Web Conf.*, **2022**, *273*, 01008

(54) Karslıoglu, O.; Trotochaud, L.; Zegkinoglou, I.; Bluhm, H. *Journal of Electron Spectroscopy and Related Phenomena*, **2018**, *225*, 55–61

(55) Harrington, G. F.; Sun, L.; Yildiz, B.; Sasaki, K.; Perry, N. H.; Tuller, H. L. The Interplay and Impact of Strain and Defect Association on the Conductivity of Rare-Earth Substituted Ceria. *Acta Materialia* **2019**, *166*, 447–458. https://doi.org/10.1016/j.actamat.2018.12.058.

(56) Marrocchelli, D.; Perry, N. H.; Bishop, S. R.; Understanding Chemical Expansion in Perovskite-Structured Oxides. *Phys. Chem. Chem. Phys.* **2015**, *17*, 10028-10039. https://doi.org/10.1039/C4CP05885B.

(57) Yim, W. M.; Paff, R. J. Thermal Expansion of AlN, sapphire, and silicon. *J. Appl. Phys.* **1974**, *45*, 1456–1457. https://doi.org/10.1063/1.1663432.